Available online at www.sciencedirect.com

SciVerse ScienceDirect

Acta Materialia 61 (2013) 5223–5235

Acta MATERIALIA

www.elsevier.com/locate/actamat

# Phase field modeling of the tetragonal-to-monoclinic phase transformation in zirconia

Mahmood Mamivand [a,b], Mohsen Asle Zaeem [c,*], Haitham El Kadiri [a,b], Long-Qing Chen [d]

[a] Center for Advanced Vehicular System, Mississippi State University, Starkville, MS 39762, USA
[b] Department of Mechanical Engineering, Mississippi State University, Starkville, MS 39762, USA
[c] Department of Materials Science and Engineering, Missouri University of Science and Technology, Rolla, MO 65409, USA
[d] Department of Materials Science and Engineering, Pennsylvania State University, University Park, PA 16802, USA

Received 14 February 2013; received in revised form 9 May 2013; accepted 15 May 2013
Available online 13 June 2013

**Abstract**

The allotropic phase transformation in zirconia from the tetragonal to monoclinic double lattices is known to occur by a martensitic twinning mechanism which shows a complex dependence on temperature, stress and environment. This paper is concerned with the development of a phase field model which accounts for the main metallurgical mechanisms governing this martensitic transition. The symmetry reduction and orientation relationship between the parent and product phases were simulated using several non-conserved order parameters representing different transformation paths. Inhomogeneous and anisotropic elastic properties were considered to determine the resultant elastic stresses. Governing equations of the tetragonal-to-monoclinic transformation were solved in a finite element framework under a variety of initial and boundary conditions. It was shown that applying different initial conditions, such as seed embryo or random, did not change the twinning patterns or the final volume fractions of the parent and product phases after the relaxation period. On the other hand, enforcing different boundary conditions resulted in completely different twinning patterns and phase volume fractions. The model was able to predict both the "V" shape morphology of twinning and the surface stress relief with "gable roof" patterns, which were observed by transmission electron microscopy and atomic force microscopy to be characteristic of the tetragonal-to-monoclinic transition.


*Keywords:* Tetragonal-to-monoclinic transformation; Zirconia; Phase field modeling

## 1. Introduction

During the last century, stabilized zirconia ceramics with tetragonal and cubic variants have become one of the most important ceramic materials for applications that require a combination of strength, fracture toughness, low thermal conductivity and good ionic conductivity. Uses of these materials include low-temperature applications such as hip joint prostheses in biomedicine and high-temperature applications such as thermal barrier coatings in jet engines and electrolytes in solid oxide fuel cells [1].

However, this unusual range of excellent properties mediated by the metastable tetragonal (or cubic) phase may systematically degenerate via an undesirable transformation to the stable monoclinic phase after a certain exposure at service temperatures. This transformation from tetragonal to monoclinic (T → M), known as LTD (low-temperature degradation) in biomedical applications, proceeds via the propagation of martensite, which corresponds to transformation twinning [1]. As such, the T → M transformation is highly sensitive to mechanical and chemomechanical stresses. It is known that this transformation is the source of the fracture toughening in stabilized zirconia as it occurs at the stress concentration regions ahead of the crack tip [2].

* Corresponding author. Tel.: +1 573 341 7184; fax: +1 573 341 6934.
*E-mail address:* zaeem@mst.edu (M. Asle Zaeem).

1359-6454/$36.00 
http://dx.doi.org/10.1016/j.actamat.2013.05.015

Another example of zirconia aging due to the T → M transformation occurs in the thermally growing oxide (TGO) over Zircaloy, used in nuclear fuel rod cladding [3]. It has been reported that TGO can be divided into two sublayers with different morphological and lattice features: a dense and very thin layer next to the metal/oxide interface mainly comprising the tetragonal variant, and an outer layer mainly comprising the monoclinic, which is highly susceptible to crack formation. As oxidation proceeds by an anionic diffusion mechanism, the new oxide molecule forms always at the oxide/metal interface, and as such the TGO zirconia grows as a tetragonal phase. Hence every molecule must undergo the T → M transformation at a certain distance from the interface [4]. Previous studies showed that the T → M transformation in the zirconium oxide layer is an important factor in corrosion degradation and crack formation in the oxide outer layer [5] and so on.

In light of this important role that the T → M transformation plays in the degradation of many zirconia ceramics, one can understand why this transformation has been the most documented allotropic transition in the ceramics literature.

For decades two different modeling approaches have been adopted in studying the T → M transformation: thermodynamic-based models and crystallographic-based models. Each of these approaches explains some aspects of the T → M transformation. Thermodynamic-based models [5–9] mainly provide some information about the onset of transformation temperature during cooling or heating, and account for the effect of grain size on the transformation kinetics. On the other hand, crystallographic phenomenological theory [10–15] is mainly capable of capturing the crystallography of transformation, such as the habit planes and the orientation relationship between the parent and product phases. None of these approaches, however, is capable of predicting the transformation kinetics and volume fraction of the parent and products at different temperatures. They can simulate neither the effects of boundary constraints on the transformation patterns nor the size and shape of product phases.

Recently, the phase field method has become a powerful computational tool for simulating different microstructures obtained by, for example, solidification [16–19], solid-state phase transformation [19–21], precipitate growth and coarsening [22,23], martensitic phase transformations (MPTs) [24] and grain growth [25,26]. Phase field models describe a microstructure by using a set of conserved and nonconserved field variables that are continuous across the interfacial regions. The temporal and spatial evolution of the field variables are governed by the Cahn–Hilliard nonlinear diffusion equation [27] and the Allen–Cahn (time-dependent Ginzburg–Landau) relaxation equation [28,29]. With the fundamental thermodynamic and kinetic information as the input, the phase field method is able to predict the evolution of arbitrary morphologies and complex microstructures without explicitly tracking the positions of interfaces [30].

The phase field method has been used for different MPTs [24,31,32]. A comprehensive review of different approaches in phase field modeling of MPTs has been recently reported by the present authors [33]. This paper uses an approach which primarily relies on developments by Khachaturyan, Chen and Wang [20,24]. Wang and Khachaturyan [24] presented the first three-dimensional (3-D) model for generic cubic-to-tetragonal improper MPT, which occurs mostly in ceramics. In a constrained single crystal, their model was able to predict the major structural characteristics of martensite during the entire transformation, including nucleation, growth and eventually formation of internally twinned plates in thermoelastic equilibrium conditions with the parent phase.

Hexagonal-to-orthorhombic transformation has also been subject to phase field modeling [34,35]. On the one hand, these models captured the effect of elastic interactions on the domain formation and evolution during nucleation, growth and coarsening. On the other hand, the effect of an applied strain field on the development of domain structure was studied. The models generally led to a good prediction of the so-called special patterns transformation, such as fan- and star-shape precipitates.

Another parameter of pronounced importance in MPT relates to the effect of externally applied stresses. Authors such as Artemev et al. [36] incorporated this effect to simulate generic improper cubic-to-tetragonal MPT. They showed in fact a noticeable increase in the product variants having transformation strain aligned with the externally applied stresses. The morphology of martensite particles was also affected. In a different paper, Artemev et al. [37] simulated proper MPT for two different types of cubic-to-tetragonal transformation, with and without volumetric change in constrained and unconstrained systems. Later on they developed a phase field model to describe a proper cubic-to-tetragonal MPT in a polycrystalline Fe–31 at.% Ni alloy under an applied stress [38].

Other models which captured the effect of externally applied stresses were developed and used to simulate the cubic-to-trigonal transformation in both single crystal and polycrystalline AuCd [39]. In this regard, the effect of free surface (vanishing external stress at boundaries) on the kinetics and topology of multivariant proper MPT was also studied via phase field modeling [40]. These models were applied to polycrystals Au–49.5 at.% Cd and Fe–31 wt.% Ni, which undergo cubic → trigonal and face-centred cubic → body-centered cubic (fcc → bcc) transformations, respectively. The phase field simulations showed inhomogeneities of martensite microstructures as a result of concentration gradients and preferential formation of martensite near free surfaces. This trend was substantiated by the stronger sensitivity of high-symmetry FeNi structures compared to low-symmetry AuCd, which has more orientation variants and can better accommodate stresses.

The effect of magnetic field on cubic-to-tetragonal transformation was studied by means of phase field modeling, which was benchmarked for $Ni_2MnGa$ material [41]. Phase field modeling also was used to study kinetics and morphologies of cubic-to-tetragonal proper MPT in thin films [42,43] and forward and reverse proper MPT [44].

Guo et al. [45] developed an elastoplastic phase field modeling for microstructure evolution and this model was used in Ref. [46] to investigate cubic-to-tetragonal transformation; the model confirmed that plastic accommodation largely reduces the elastic strain energy during the formation of the tetragonal phase because of both self and plastic accommodations.

The above review shows that substantial research was recently performed to utilize the phase field approach in studying cubic-to-tetragonal MPT [24,36–38,41–43,46,47]. However, to the best of our knowledge, there exists no phase field model for simulating the T → M transformation in zirconia. In this study, we present a phase field model for this phase transformation which is anisotropic and inhomogeneous elastically. The paper is organized as follows: Section 2 describes the thermodynamics of the T → M transformation; Section 3 describes the crystallography of the T → M transformation; Section 4 presents the process of developing the governing equations of the phase field model for the T → M transformation; and Section 5 presents and discusses the simulation results for different initial and boundary conditions, and comparison to experimental results.

## 2. Thermodynamics of the T → M transformation

Solid-state phase transformations can be diffusional or diffusionless. In diffusional transformations, long-range diffusion is required for the growth of the new phases; however, in diffusionless transformations, atoms move only short distances in order to join the new phases. The T → M transformation takes place by a diffusionless mechanism [48]. Diffusionless transformations are classified into two types: (1) massive, which takes place without a definite orientation relationship and atoms can move individually; and (2) martensitic, in which atoms have to move in a coordinated manner so there is a shape change in crystal associated with transformation strains. The nature of the diffusionless T → M transformation has been classified as martensitic transformation. The martensitic nature of the T → M transformation was first suggested by Wolten [49].

Wang et al. [50] calculated equilibrium temperature for the T → M phase transformation for pure zirconia and adopted it for the assessment of Gibbs free energy of zirconia in different phases. According to Ref. [50], the equilibrium temperature is a temperature at which the Gibbs free energy of both tetragonal and monoclinic phases are the same; this temperature for the T → M transformation is 1367 ± 5 K, and the Gibbs free energies for monoclinic and tetragonal zirconia are:

$$GZrO_2M = -1126163.5 + 424.8908T - 69.38751T\ln T - 0.0037588T^2 + 683000T^{-1} \quad (1)$$

$$GZrO_2T = 5468 - 4T + GZrO_2M \quad (2)$$

where the Gibbs free energies are in J mol$^{-1}$, and the temperature ($T$) is in Kelvin.

## 3. Crystallography of the T → M transformation

Zirconia exhibits three polymorphs: cubic, tetragonal and monoclinic. The cubic phase is stable for temperatures above 2640 K to the melting point, and has a fluorite type structure with a unit cell dimension of $a_c = 5.27$ Å [1] (Fig. 1).

The tetragonal phase is stable for temperatures above 1430 K and below 2640 K. The primitive tetragonal unit cell has two $ZrO_2$ units, unlike cubic fluorite and monoclinic unit cells (which have four $ZrO_2$ units), so it is more convenient to describe the tetragonal unit cell in terms of the C-centered tetragonal unit cell, which has four $ZrO_2$ (Fig. 2). The C-centered tetragonal zirconia lattice parameters are $a_t = 5.14$ Å and $c_t = 5.26$ Å [51].

The monoclinic phase is stable from room temperature to temperatures below 1430 K. The crystal structure of the monoclinic phase revealed the unit cell parameters to be $a_m = 5.184$ Å, $b_m = 5.207$ Å and $c_m = 5.370$ Å with $\beta_m = 98.8°$ ($\beta_m$ is the angle between $a_m$ and $c_m$) [51] (Fig. 3).

As mentioned before, the T → M transformation is martensitic in nature. There are three different correspondences for the T → M transformation (each correspondence shows which atom at the parent structure becomes which atom at a product phase) [15]. If ($a_t$, $b_t$, $c_t$) and ($a_m$, $b_m$, $c_m$) represent tetragonal and monoclinic lattice parameters, respectively, the product correspondences are:

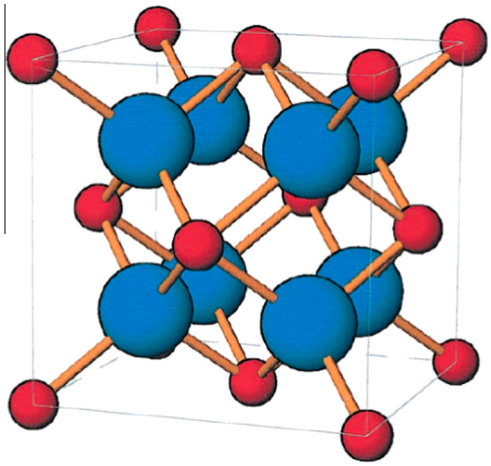

Fig. 1. Schematic of cubic zirconia crystal structure (red atoms are zirconium and blue ones are oxygen) [2]. (For interpretation of the references to color in this figure legend, the reader is referred to the web version of this article.)

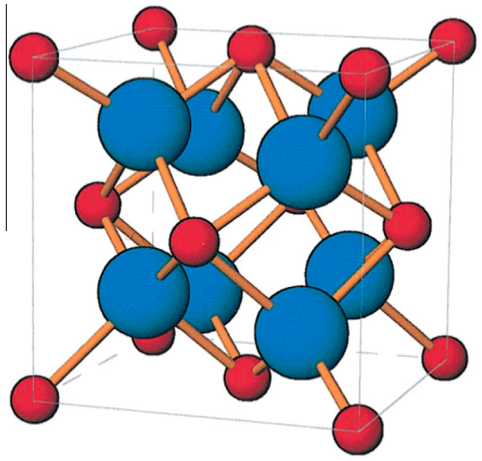

Fig. 2. Schematic of tetragonal zirconia crystal structure (red atoms are zirconium and blue ones are oxygen) [2]. (For interpretation of the references to color in this figure legend, the reader is referred to the web version of this article.)

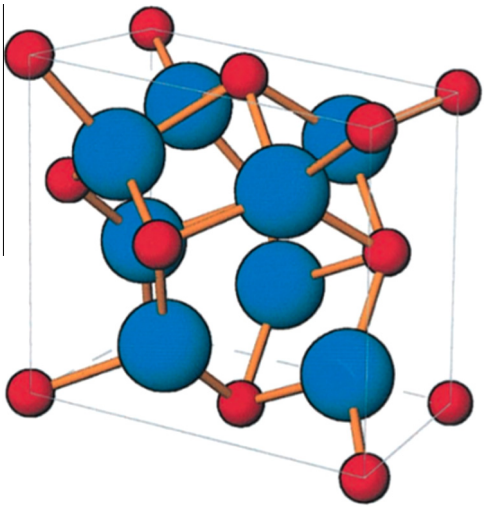

Fig. 3. Schematic of monoclinic zirconia crystal structure (red atoms are zirconium and blue ones are oxygen) [2]. (For interpretation of the references to color in this figure legend, the reader is referred to the web version of this article.)

$$T \rightarrow M \text{ correspondences} \begin{cases} ABC: \text{ if } (a_t, b_t, c_t) \rightarrow (a_m, b_m, c_m) \\ CAB: \text{ if } (a_t, b_t, c_t) \rightarrow (c_m, a_m, b_m) \\ BCA: \text{ if } (a_t, b_t, c_t) \rightarrow (b_m, c_m, a_m) \end{cases}$$

We know that $a_t = b_t$. These correspondences were named in early literature based on the counterpart of $c_t$, which means that the first correspondence was named $C$ because $c_t$ becomes $c_m$, and the second correspondence was named $B$ because $c_t$ becomes $b_m$, and in the same way the last correspondence was named $A$.

For each correspondence there are two variants. Variants are crystallographically equivalent, but rotated with respect to each other. For example, consider correspondence $B$; in this case $c_t$ becomes $b_m$ but for the other axes ($a_t$, $b_t$), there are two situations: (1) $a_t \rightarrow a_m$ and $b_t \rightarrow c_m$, (2) $b_t \rightarrow a_m$ and $a_t \rightarrow -c_m$ (using a right-handed set of axes), which we can represent by $ACB$ and $\overline{C}AB$ to distinguish variants in transformation. These variants are crystallographically equivalent, but rotated 90° around the $c_t$ axis.

Unlike the tetragonal crystal with orthogonal axes, the angle between $a_m$ and $c_m$ axes in the monoclinic crystal is ~99°, so the axes of the parent and product cannot lie on each other. Since $b_m$ is perpendicular to the plane of $c_m$ and $a_m$, and if we keep $b_m$ parallel to its counterpart parent axis, there are two options for the two remaining axes ($c_m$, $a_m$): (1) $a_m$ becomes parallel to its counterpart axis and $c_m$ incline by $9^0$ from parent axis, (2) $c_m$ becomes parallel to its counterpart parent axis and $a_m$ become inclined. Hence for each variant there are two possible orientation relationships, which gives six possible orientations in total: $A1$, $A2$, $B1$, $B2$, $C1$ and $C2$ [15]. For the T → M transformation, there are three correspondences, each of which has two variants, and each variant has two orientations. In total, for each tetragonal lattice there are 12 possible lattices in the monoclinic phase. Fig. 4 illustrates the different variants and orientations of correspondence $ABC$.

Among possible correspondences, $C$ and $B$ are more favored because they have the smallest Bain strain and lattice invariant strain, respectively. In correspondence $A$, because of $c_t \rightarrow a_m$, we have the largest Bain strain, so this correspondence is rare and the T → M transformation follows either correspondence $B$ or correspondence $C$ [15].

## 4. Phase field modeling of the T → M transformation

In the phase field method, a multidomain microstructure can be described by a set of phase field variables. In the case of the T → M phase transformation, phase field variables are the possible variants of the monoclinic phase.

The temporal and spatial evolution of non-conserved phase-field variables are described by the phenomenological time-dependent Ginzburg–Landau kinetic equation [29]:

$$\frac{\partial \eta_p(\vec{r}, t)}{\partial t} = -L \frac{\delta F}{\delta \eta_p(\vec{r}, t)} + \varsigma_p(\vec{r}, t) \qquad p = 1, \ldots, n \tag{3}$$

where $\eta_p$ represent the $p$th variant of monoclinic, $L$ is the kinetic coefficient, $F$ is the total free energy of the system, $\delta F/\delta \eta_p(\vec{r}, t)$ is the thermodynamic deriving force for spatial and temporal evolution of $\eta_p$ and $\varsigma_p(\vec{r}, t)$ is the Langevin noise describing the thermal fluctuation [24,52]. The value of $\eta_p$ varies from 0 to 1; where $\eta_p = 1$, the $p$th variant of monoclinic exists, and where $\eta_p = 0$, it could be the other variants or the parent phase.

For an MPT, the total free energy can be written as the summation of chemical free energy and elastic strain energy:

$$F = F_{ch} + F_{el} \tag{4}$$

### 4.1. Chemical free energy

The driving force of an MPT comes from chemical free energy. The total chemical free energy can be written as [24]:

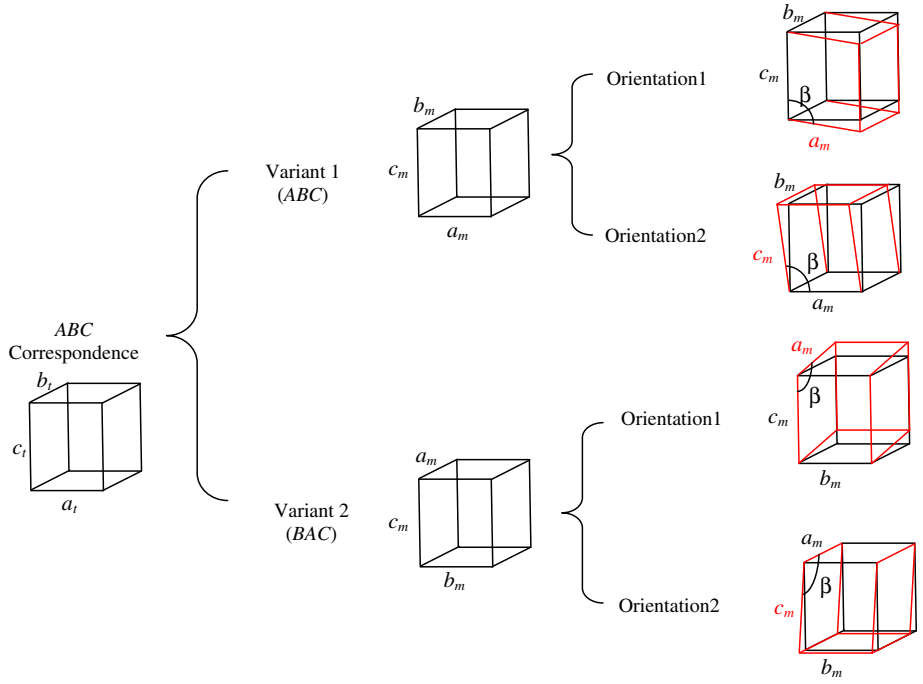


Fig. 4. Different variants and orientations of correspondence *ABC*.

$$F_{ch} = \int_V \left[ f(\eta_1, \eta_2, \ldots, \eta_n) + \frac{1}{2}\sum_{p=1}^{n} \beta_{ij}(p) \nabla_i \eta_p \nabla_j \eta_p \right] dV$$
$$n = 1, \ldots, p \tag{5}$$

where $\beta_{ij}(p)$ is a positive gradient energy coefficient and $\nabla$ is the gradient operator. $f(\eta_1, \eta_2, \ldots, \eta_n)$ is the local specific free energy, which defines the basic bulk thermodynamic properties of the system. $f(\eta_1, \eta_2, \ldots, \eta_n)$ can be approximated by the Landau polynomial in terms of long-range order parameters $\eta_p$. Since elastic energy and domain wall energy determine the domain structure after the transformation is completed, the particular form of the free energy model has no significant effect on the domain structure [34]; therefore we selected the simplest sixth-order polynomial form for the local specific free energy:

$$f(\eta_1, \eta_2, \ldots, \eta_n) = \Delta G \left[ \frac{a}{2}\left(\eta_1^2 + \eta_2^2 + \ldots + \eta_n^2\right) - \frac{b}{4}\left(\eta_1^4 + \eta_2^4 + \ldots + \eta_n^4\right) + \frac{c}{6}\left(\eta_1^2 + \eta_2^2 + \ldots + \eta_n^2\right)^3 \right] \tag{6}$$

where $\Delta G$ is the chemical driving force representing the difference in the specific chemical free energy between the parent and the equilibrium martensitic phase. $\Delta G$ is calculated using Eqs. (1) and (2). $a$, $b$ and $c$ are the expansion coefficients at a fixed temperature, and although they are not dominant in microstructure evolution, they must be selected in a way that (1) maintains the same value of the interfacial energy within the physical reasonable range and (2) provides global minima at the parent phase ($\eta_1 = \eta_2 = \cdots = \eta_n = 0$) and at all the product variants, which are

$$\eta_1 = \pm\eta_0, \quad \eta_2 = \eta_3 = \cdots = \eta_n = 0,$$
$$\eta_2 = \pm\eta_0, \quad \eta_1 = \eta_3 = \cdots = \eta_n = 0,$$
$$\vdots$$
$$\eta_n = \pm\eta_0, \quad \eta_1 = \eta_2 = \cdots = \eta_{n-1} = 0,$$

where $\eta_0 \neq 0$ is the equilibrium long-range parameter and usually considered to take the value 1.

We assume that the positive gradient energy coefficient is isotropic ($\beta_{ij} = \beta\delta_{ij}$); therefore the chemical free energy can be simplified as:

$$F_{ch} = \int_V \left[ f(\eta_1, \eta_2, \ldots, \eta_n) + \frac{1}{2}\sum_{p=1}^{n} \beta (\nabla_i \eta_p)^2 \right] dV \tag{7}$$

### 4.2. Elastic strain energy

In MPT, an important contribution to the total free energy comes from the strain energy caused by the lattice mismatch between the product precipitates and the parent matrix. It has been shown by Khachaturyan [53] that strain energy can be expressed as a function of the transformation-induced stress-free strain $\varepsilon_{ij}^0(\vec{r})$. In fact, the degree of lattice mismatch between precipitates and the matrix can be characterized by stress-free strain. Because of our diffusive interface description, we need to express the stress-free strain in terms of phase field variables; therefore the local stress-free strain is related to order parameters through [24]:

$$\varepsilon_{ij}^0(\vec{r}) = \sum_{p=1}^{n} \varepsilon_{ij}^{00}(p) \eta_p^2(\vec{r}) \tag{8}$$

where $\varepsilon_{ij}^{00}(p)$ is the transformation strain of the $p$th variant. The elastic strain energy of a system is given by:

$$F_{el} = \frac{1}{2}\int_V \sigma_{ij}\varepsilon_{ij}^{el} dV = \frac{1}{2}\int_V C_{ijkl}\varepsilon_{kl}^{el}\varepsilon_{ij}^{el} dV \tag{9}$$

where the elastic strain $\varepsilon_{ij}^{el}(\overrightarrow{r})$ is the difference between the total strain, $\varepsilon_{ij}^{tot}(\overrightarrow{r})$, and the stress-free strain, $\varepsilon_{ij}^{0}(\overrightarrow{r})$:

$$\begin{aligned}\varepsilon_{ij}^{el}(\vec{r}) &= \varepsilon_{ij}^{tot}(\vec{r}) - \varepsilon_{ij}^{0}(\vec{r}) = \varepsilon_{ij}^{tot}(\vec{r}) - \sum_p \varepsilon_{ij}^{00}(p)\eta_p^2(\vec{r}) \\ &= \frac{1}{2}\left(\frac{\partial u_i(\overrightarrow{r})}{\partial r_j} + \frac{\partial u_j(\overrightarrow{r})}{\partial r_i}\right) - \sum_p \varepsilon_{ij}^{00}(p)\eta_p^2(\overrightarrow{r})\end{aligned} \tag{10}$$

Stress-free strain, which has different names in the literature such as transformation strain [54], eigenstrain [55] or Bain strain [56], is the strain that occurs inside the material during phase transformation in the absence of external constrains. In MPT, each variant has its own stress-free strain and can be calculated from lattice parameters of parent and product. For small strains the transformation strain is [54]:

$$\varepsilon_{ij}^{00}(p) = U_{ij}(p) - \delta_{ij} \tag{11}$$

where $U_{ij}(p)$ is the symmetric right stretch tensor of the deformation gradient which maps the parent crystal to the $p$th variant of the product. In two dimensions, the smallest transformation strain is for correspondence $ABC$. Fig. 5 shows possible monoclinic variants of correspondence $ABC$ in two dimensions and Tables 1 and 2 show the lattice parameters of zirconia and transformation strain tensors for correspondence $ABC$, respectively.

### 4.3. Evolution equations

The Ginzburg–Landau equation for the T → M transformation with the energy function given in the previous section is:

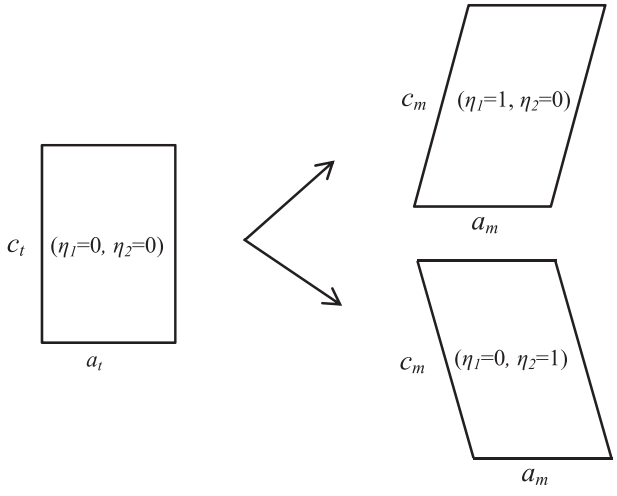


Fig. 5. Possible variants of monoclinic phase in the T → M phase transformation in two dimensions.

Table 1
Lattice parameters for tetragonal and monoclinic zirconia [49].

| Crystal parameter | $a$ | $b$ | $c$ | $\beta$ |
|---|---|---|---|---|
| Tetragonal | 5.141 | 5.141 | 5.2609 | 90° |
| Monoclinic | 5.184 | 5.207 | 5.370 | 98.8° |

$$\begin{aligned}\frac{\partial \eta_p(\vec{r},t)}{\partial t} &= -L\left(-\beta\nabla^2\eta_p(\vec{r},t) + \frac{\partial f}{\partial \eta_p(\vec{r},t)} + \frac{\delta F_{el}}{\delta \eta_p(\vec{r},t)}\right) \\ &\quad + \varsigma_p(\vec{r},t) \qquad p = 1,\ldots,n\end{aligned} \tag{12}$$

where $f$ was defined in Eq. (6), and

$$\begin{aligned}\frac{\delta F_{el}}{\delta \eta_p(\overrightarrow{r},t)} &= -\frac{1}{2}C_{ijkl}\varepsilon_{kl}^{00}(p)\eta_p(\overrightarrow{r},t)(u_{i,j}(\overrightarrow{r}) + u_{j,i}(\overrightarrow{r})) \\ &\quad + C_{ijkl}\varepsilon_{kl}^{00}(p)\eta_p(\overrightarrow{r},t)\sum_{z=1}^{n}\varepsilon_{ij}^{00}(z)\eta_z^2(\overrightarrow{r},t) \\ &\quad - \frac{1}{2}C_{ijkl}\varepsilon_{ij}^{00}(p)\eta_p(\overrightarrow{r},t)(u_{k,l}(\overrightarrow{r}) + u_{l,k}(\overrightarrow{r})) \\ &\quad + C_{ijkl}\varepsilon_{ij}^{00}(p)\eta_p(\overrightarrow{r},t)\sum_{z=1}^{n}\varepsilon_{kl}^{00}(z)\eta_z^2(\overrightarrow{r},t)\end{aligned} \tag{13}$$

The Ginzburg–Landau equations are coupled to the mechanical equilibrium equations to find the displacement of domain:

$$\frac{\partial \sigma_{ij}}{\partial r_j} = 0 \Rightarrow C_{ijkl}\left[\frac{1}{2}(u_{k,lj}(\overrightarrow{r}) + u_{l,kj}(\overrightarrow{r})) - \sum_p \varepsilon_{kl}^{00}(p)\frac{\partial}{\partial r_j}(\eta_p^2(\vec{r}))\right] = 0 \tag{14}$$

## 5. Results and discussion

In this work, we studied the T → M phase transformation in a two-dimensional (2-D) single crystal; 2 μm × 2 μm square domains were used in all the simulations, except in Section 5.3 where a 3 μm × 3 μm domain was used. We considered the Langevin noise to be zero and imposed two different initial conditions for order parameters: (1) randomly distributed initial condition, and (2) multivariant martensitic embryo initial condition. The initial condition for displacement is zero in the whole domain, and boundary conditions for the $i$th order parameter are periodic and

$$n \cdot \nabla\eta_i = 0, \ \ i = 1,\ldots,p \tag{15}$$

The boundary conditions for the mechanical equilibrium Eq. (14) at all the boundaries are:

$$u_1 = u_2 = 0 \tag{16}$$

The homogeneous constant temperature $T = 1170$ K was considered.

Unlike most of the phase field simulations which assumed elastic homogeneity [44,46,57–60], we considered inhomogeneous elasticity and defined a smooth T → M transition with elastic constants given by the following equation:

Table 2
Deformation gradient ($F_{ij}$), right stretch tensor ($U_{ij}$) and transformation strain ($\varepsilon^{00}_{ij}$) of monoclinic variants.

| Correspondence | $F_{ij}$ | $U_{ij}$ | $\varepsilon^{00}_{ij}$ | $\varepsilon^{00}_{ij}$ for self-accommodating variant |
|---|---|---|---|---|
| ABC | $\begin{bmatrix} \frac{a_m}{a_t} & \frac{-c_m\cos(\beta)}{c_t} \\ 0 & \frac{c_m\sin(\beta)}{c_t} \end{bmatrix}$ | $\begin{bmatrix} 1.0049 & 0.0761 \\ 0.0761 & 1.0180 \end{bmatrix}$ | $\begin{bmatrix} 0.0049 & 0.0761 \\ 0.0761 & 0.0180 \end{bmatrix}$ | $\overline{ABC}\begin{bmatrix} 0.0049 & -0.0761 \\ -0.0761 & 0.0180 \end{bmatrix}$ |

$$C = P\left(\sum_{i=1}^{n}\eta_i\right)C^M + \left(1 - P\left(\sum_{i=1}^{n}\eta_i\right)\right)C^T \tag{17}$$

where $C^M$ and $C^T$ are monoclinic and tetragonal elastic constants, respectively, $n$ is the number of order parameters and

$$P(\eta) = \eta^3(6\eta^2 - 15\eta + 10) \tag{18}$$

In previous works, we developed a mixed-order finite element model for the coupled phase field equation and elasticity equations to study solid-state phase transformations [19,23,61,62]. Although in the present work all the equations in the model are second order partial differential equations (PDEs), a similar algorithm was adopted. We used COMSOL Multiphysics to solve the PDEs [63]. The calculation domain was discretized by 10,000 four-noded quadratic rectangular elements, and the whole system had 161,604 degrees of freedom. For time integration, an adaptive time-step algorithm was implemented; at the initial stages of the growth, time steps less than $3 \times 10^{-11}$ s were used to guarantee the convergence of the solution, and at the later stages of growth, time steps less than $2 \times 10^{-9}$ s were sufficient to ensure the convergence.

The input parameters of the model are given in Tables 3–5.

### 5.1. Evolution of the monoclinic with random initially distributed order parameters

In this section, the evolution of the monoclinic phase is investigated for cases with randomly distributed order parameters as their initial condition. First, a Gaussian random distribution from 0 to 1 was assigned to one variant as the initial condition and the other order parameters were kept zero throughout the system initially. In this case, the MPT did not start, and it showed that the presence of two twin related variants are necessary for martensitic nucleation; a similar result was suggested in Refs. [24,37]. In our second try, we assigned a Gaussian random distribution from 0 to 0.5 to both order parameters as their initial conditions and set the boundary condition clamped. The results showed that in the initial steps there are several nuclei which have the same chance to grow, but the system only allows the growth of critical nuclei (the nuclei having both twin related variants) and the non-critical nuclei eventually disappear; similar results for MPT of cubic to tetragonal was reported in Ref. [24].

Table 4
Elastic constants for tetragonal zirconia (GPa) [4,63].

| $C_{11}$ | $C_{33}$ | $C_{44}$ | $C_{66}$ | $C_{12}$ | $C_{13}$ |
|---|---|---|---|---|---|
| 327 | 264 | 59 | 64 | 100 | 62 |

Table 5
Numerical values used for calculation.

| Temperature (K) | 1170 |
|---|---|
| Chemical driving force (J mol$^{-1}$) | 800 ($36.8 \times 10^6$ J m$^{-3}$) |
| Gradient energy coefficient, $\beta$ (J m$^{-1}$) | $1 \times 10^{-8}$ |
| Energy density coefficient, $a$ | 0.14 |
| Energy density coefficient, $b$ | 12.42 |
| Energy density coefficient, $c$ | 12.28 |
| Kinetic coefficient, $L$ (m$^3$ J$^{-1}$ s$^{-1}$) | 2 |
| Domain size (nm × nm) | 2000 × 2000 |

The temporal and special evolution of monoclinic variants ($\eta_1$, $\eta_2$) and the stresses $\sigma_{11}$ and $\sigma_{11} - \sigma_{22}$ are shown in Fig. 7. The simulation results show that the twinning plane (junction plane) is $(1\,0\,0)_m$, which is in agreement with

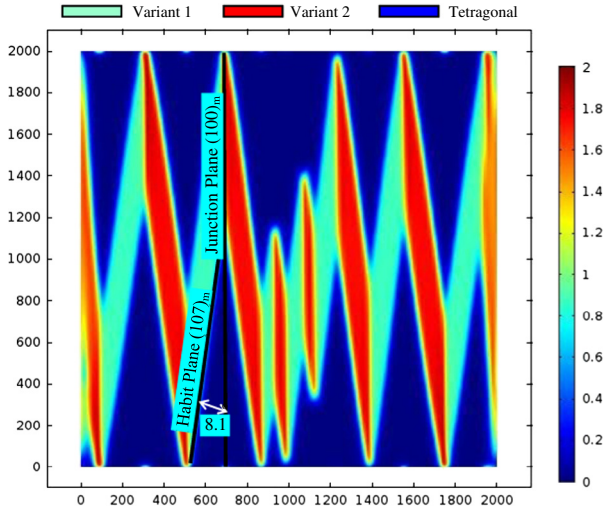


Fig. 6. Junction and habit planes predicted by simulation.

Table 3
Elastic constants for monoclinic zirconia (GPa) [4,62].

| $C_{11}$ | $C_{22}$ | $C_{33}$ | $C_{44}$ | $C_{55}$ | $C_{66}$ | $C_{12}$ | $C_{13}$ | $C_{16}$ | $C_{23}$ | $C_{26}$ | $C_{36}$ | $C_{45}$ |
|---|---|---|---|---|---|---|---|---|---|---|---|---|
| 361 | 408 | 258 | 100 | 81 | 126 | 142 | 55 | −21 | 196 | 31 | −18 | −23 |

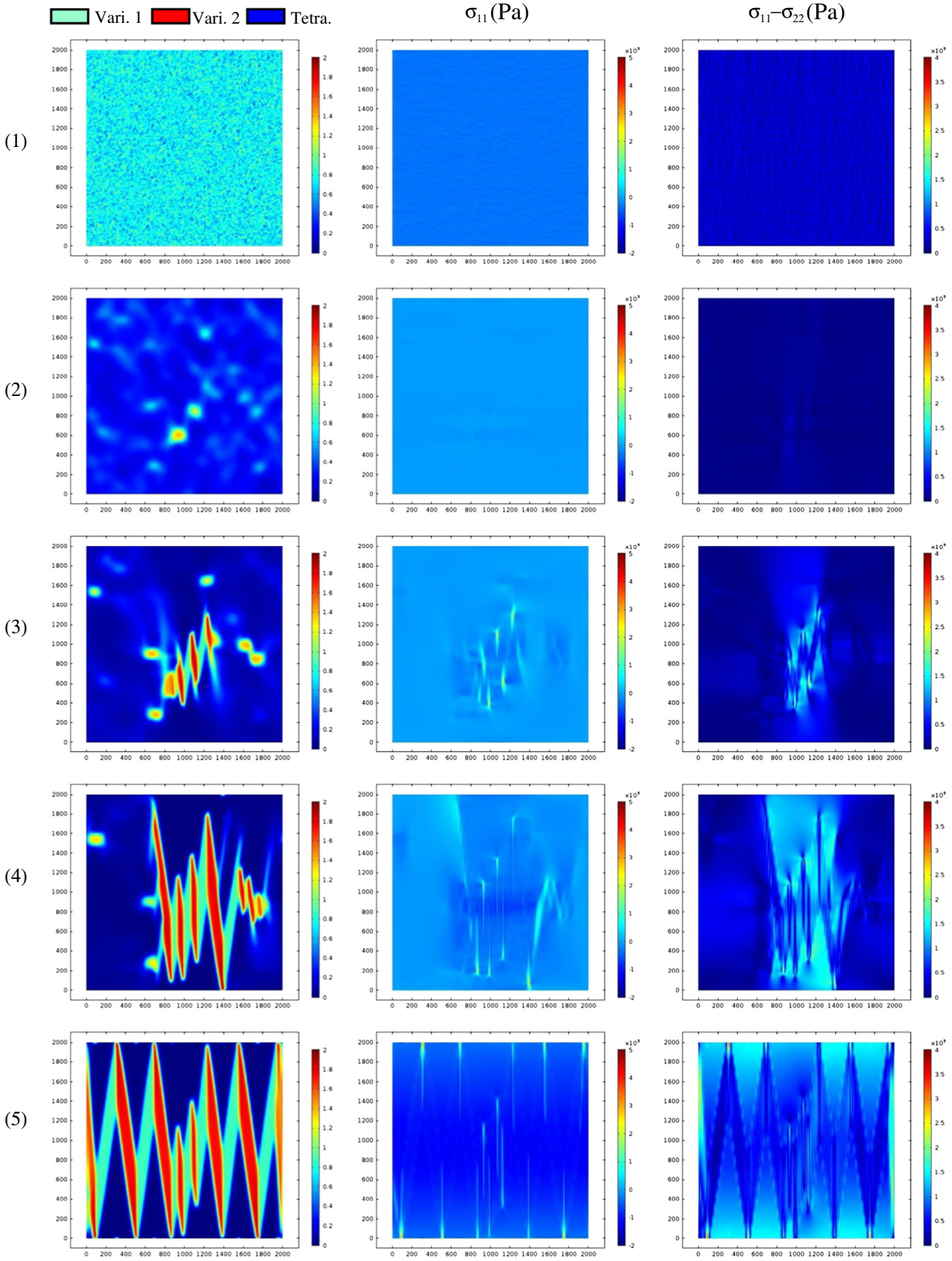


Fig. 7. Temporal and spatial evolution of monoclinic phase with initially randomly distributed order parameters and clamped boundary condition. The left column shows the evolution of monoclinic variants. The second and third columns show the evolution of $\sigma_{11}$ and $\sigma_{11} - \sigma_{22}$. Rows (1)–(5) correspond to times 0, $9 \times 10^{-8}$, $1.65 \times 10^{-7}$, $2.25 \times 10^{-7}$ and $1 \times 10^{-6}$ s, respectively.

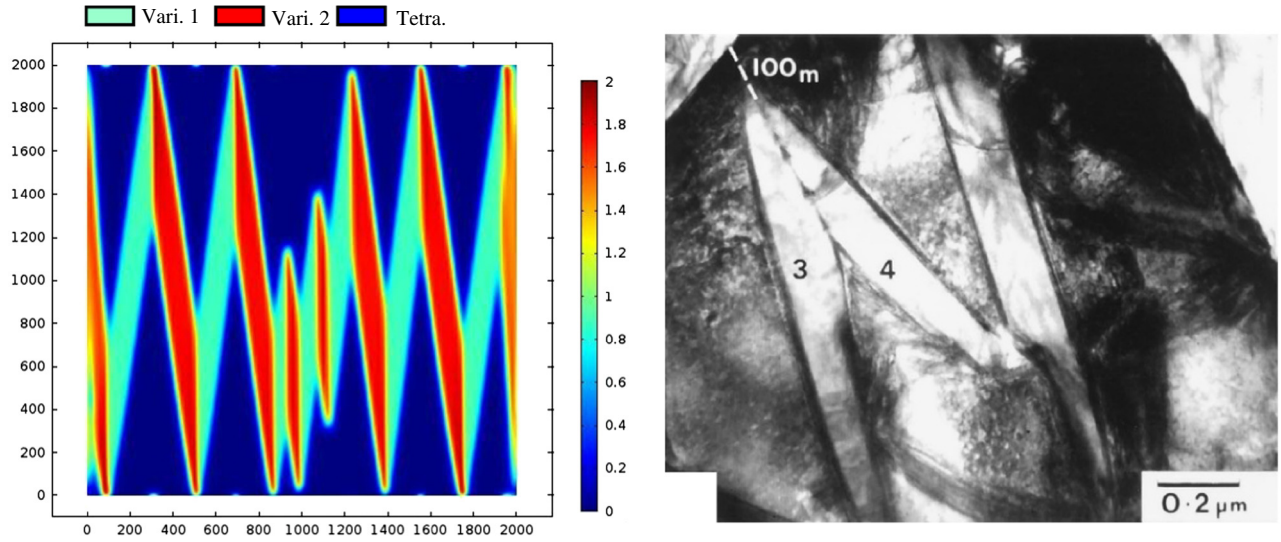


Fig. 8. Left picture is the simulation result for random initially distributed order parameters in a constrained single crystal. Right picture is a TEM micrograph of partially transformed t-$ZrO_2$ grains in $CeO_2$-stabilized polycrystalline TZP [2].

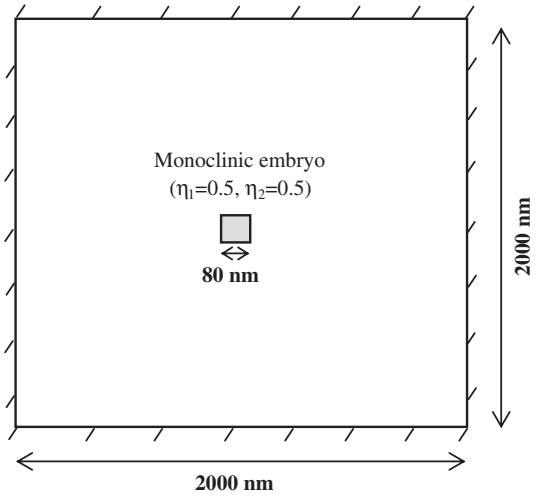


Fig. 9. A 2-D tetragonal phase with clamped boundary and multivariant embryo initial conditions.

Bansal and Heuer [10,64] observations. Simha [56] calculations also show the same result. Kelly and Rose [15] mentioned $(1\,0\,7)_m$ as a significant habit plane in the T → M phase transformation. This plane has been well predicted by simulation (Fig. 6).

Fig. 8 shows a comparison between the simulation result and an experimental transmission electron microscopy (TEM) image of the T → M; from this figure, we can see that habit planes formed as a pair of plates arranged in a "V" shape and the sequence arranged in a chain of "N" shapes. The same results based on crystallographic phenomenological theory have been reported in Ref. [15].

### 5.2. Evolution of the monoclinic with middle seed embryo

At the next step we studied the evolution of a monoclinic embryo. Fig. 9 shows the initial and boundary conditions of the tetragonal single crystal with a small multivariant monoclinic embryo in the middle.

The evolution of a single embryo is shown in Fig. 10: at the initial steps of transformation the embryo grows in both directions, then some lenticular monoclinic variants are formed in the $(1\,0\,0)_m$ plane. The variants grow and join together in a "V" type pattern. Transformation time in the single embryo initial condition is longer than randomly distributed order parameters because in the latter case transformation is triggered in several critical nuclei simultaneously.

Fig. 11 shows the growth rate of volume fraction of different variants and parent phase for the single embryo initial condition. We defined the volume fraction of each variant by the following equation:

$$VF_i = \frac{\int \eta_i dA}{A} \tag{19}$$

where $VF_i$ is the volume fraction of the $i$th variant and $A$ is the total area of the domain. In this case the system relaxed after 1.6 μs and volume fractions remained unchanged. Fig. 12 shows the volume fraction of parent and products for randomly distributed order parameter initial conditions. Unlike Fig. 11, in which the monoclinic volume fraction starts from zero and increases to the final value of 22%, in Fig. 12 because of initial disturbance the volume fraction of each monoclinic variant starts from 24%. After that the disturbance relaxes and the volume fraction decrease to 8% and then monoclinic variants start to grow from critical embryos to the final equilibrium, which is 22% for each variant. The final volume fractions in Figs. 11 and 12 show that the amount of tetragonal transformation to monoclinic does not depend on the initial condition.

### 5.3. "Gable patterns" formation on free surfaces

Atomic force microscopy (AFM) investigations [65,66] showed that the martensitic T → M transformation results

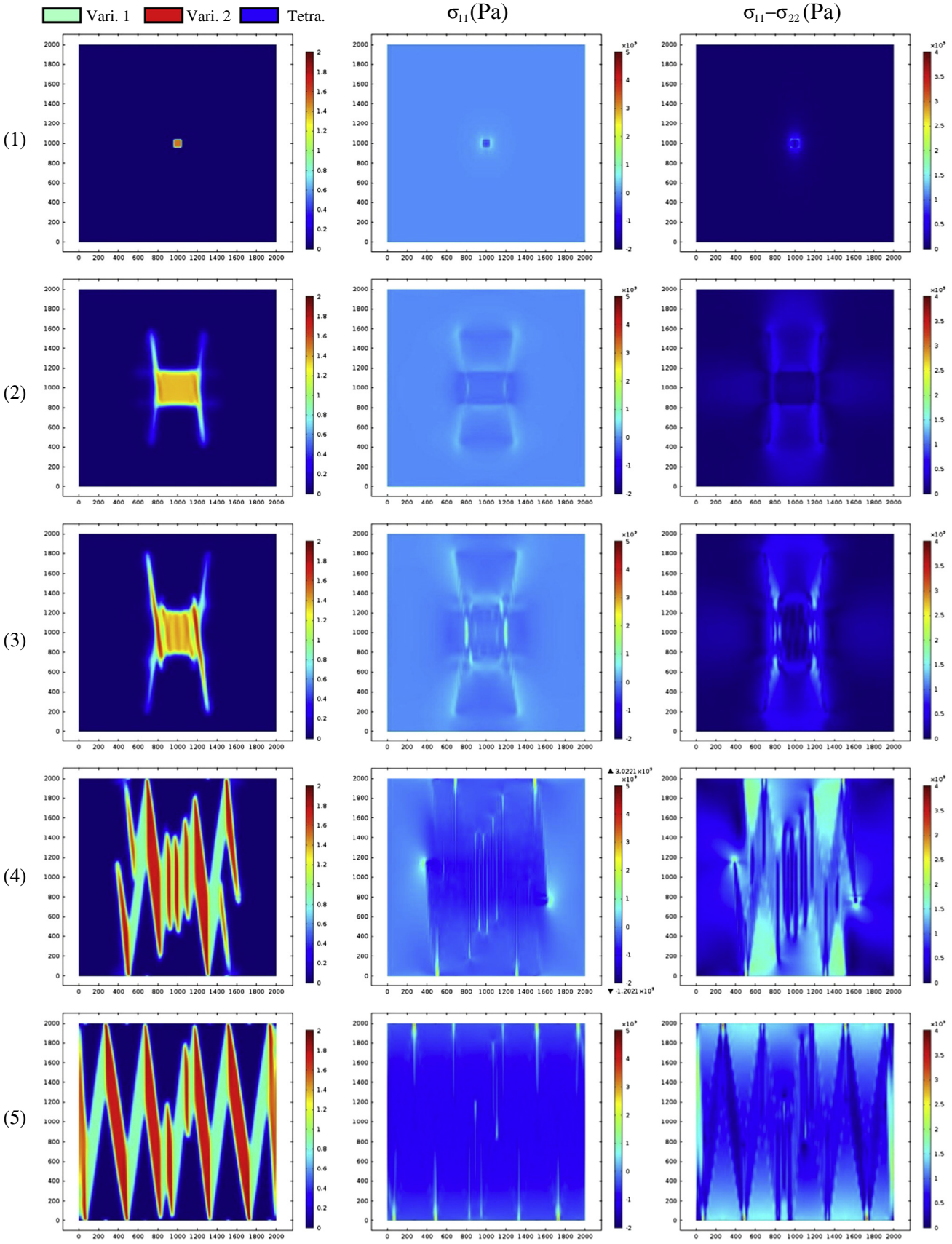


Fig. 10. Temporal and spatial evolution of monoclinic phase with initial multivariant embryo and clamped boundary conditions. The left column shows the evolution of monoclinic variants. The second and third columns show the evolution of $\sigma_{11}$ and $\sigma_{11} - \sigma_{22}$. Rows (1)–(5) correspond to times 0, $4 \times 10^{-7}$, $5 \times 10^{-7}$, $8 \times 10^{-7}$ and $2.7 \times 10^{-6}$ s, respectively.

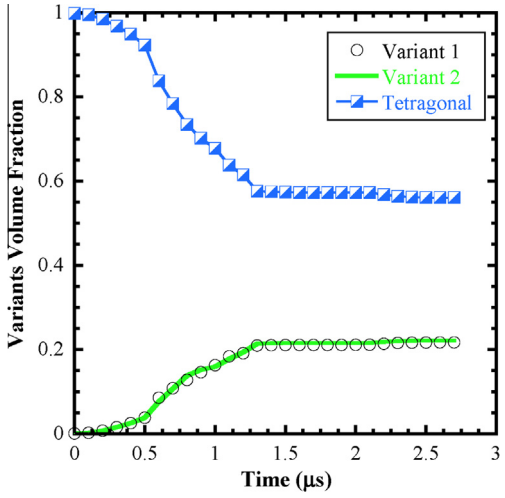


Fig. 11. Temporal evolution of parent and product volume fraction for clamped boundary condition with seed embryo initial condition.

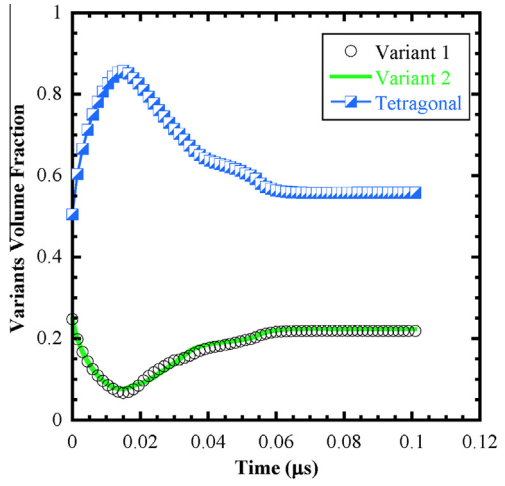


Fig. 12. Temporal evolution of parent and product volume fraction for clamped boundary condition with randomly distributed order parameter initial condition.

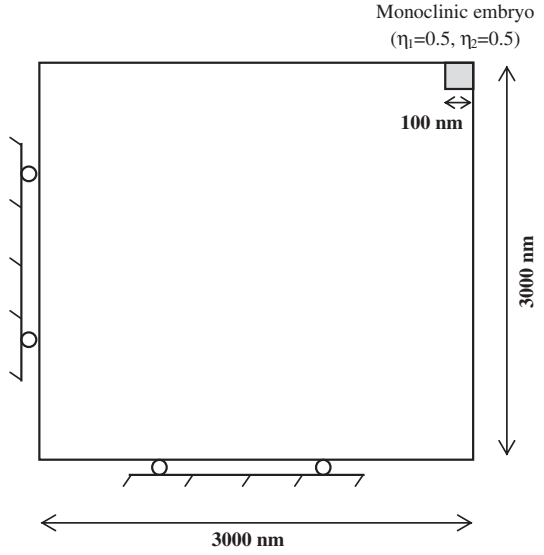


Fig. 13. Selected boundary condition to study free surfaces.

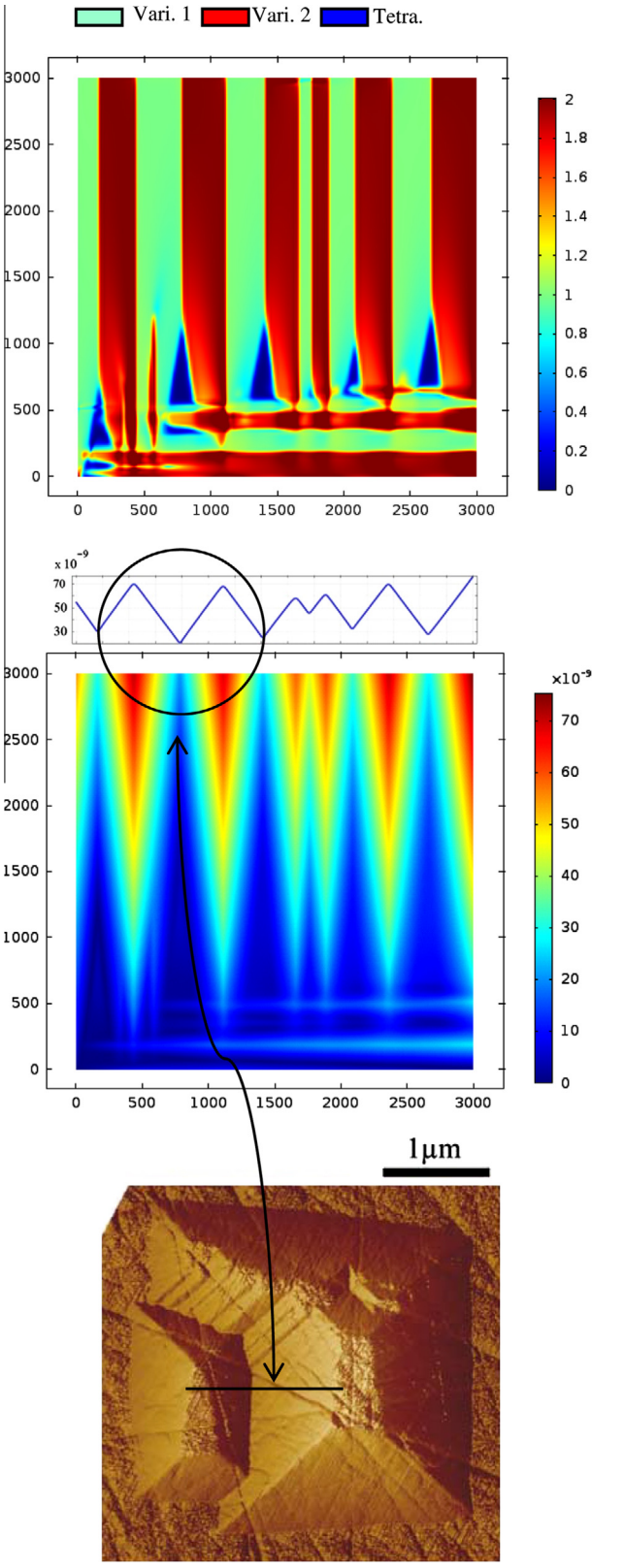


Fig. 14. The top picture shows the monoclinic evolution, the middle picture shows the displacement (color bar: 0–75 × $10^{-9}$ m) and the bottom picture is the AFM micrograph of surface relief resulting from the martensitic T → M phase transformation [67]. (For interpretation of the references to color in this figure legend, the reader is referred to the web version of this article.)

in surface relief. To investigate this phenomenon we studied the T → M transformation with free boundary conditions. A single crystal 3 μm × 3 μm square domain was discretized by 14,400 four-noded quadratic rectangular elements and the whole system had 232,324 degrees of freedom. For time integration, at the initial stages of the growth, time steps less than $1 \times 10^{-9}$ s were used to guarantee the convergence of the solution, and at the later stages of growth, time steps less than $5 \times 10^{-10}$ s were sufficient to ensure the convergence.

Fig. 13 shows the boundary conditions for displacement, and the boundary conditions for order parameters are $n \cdot \nabla \eta_i = 0,\ i = 1, \ldots, p$ with the initial embryo seed in the top right corner as the initial condition.

The unconstrained simulation shows that the T → M transformation does not produce a strain-accommodating state because the strain-accommodating multivariants do not relax the dilatational strain. This dilatational strain causes surface relief at free surfaces. For the case of variant *ABC*, when the free surface is $(001)_t$, the junction plane would be $(100)_m$, and we can see an inverse "V" come out of the free surface and its maximum is at the junction plane; the same result was reported in AFM investigations on transformation-induced relief in zirconia by Deville et al. [67]. Fig. 14 shows a comparison between surface relief results of the phase field model and experiment [67]. It needs to be noted that although variants with a $(100)_m$ junction plane are favorable, because of our restriction on the $u_2$ direction on the lower boundary, some variants of the $(001)_m$ junction plane and some small gable roof patterns on the $(100)_t$ plane are formed.

## 6. Conclusion

A 2-D phase field model was developed to predict the microstructural evolution during the T → M phase transformation in zirconia. Inhomogeneous and anisotropic elastic properties were considered in the model and governing equations were solved in a finite element framework. The model shows high fidelity as the simulation results reproduced the main crystallographic, kinetic and morphological features, which were observed by experiments to be characteristic of the transformation. For instance, the "V" type variants with $(100)_t$ junction plane observed by Hannink et al. [2] were successfully predicted. The model also predicted the "gable roof" pattern on free surfaces reported by observations using AFM. The simulation results showed that the initial condition on order parameters does not affect twinning patterns and martensitic volume fraction, which was in marked contrast to the effect of mechanical boundary conditions.

## Acknowledgements

The authors appreciate the sponsorship of the Institute for Nuclear Energy Science and Technology Laboratory Directed Research and Development (INEST LDRD) and the Center for Advanced Vehicular Systems at Mississippi State University.

## References

[1] Chevalier J, Gremillard L, Virkar AV, Clarke DR. J Am Ceram Soc 2009;92:1901.
[2] Hannink RH, Kelly PM, Muddle BC. J Am Ceram Soc 2000;83:461.
[3] El Kadiri H, Utegulov ZN, Khafzov M. Asle Zaeem M, Mamivand M, Oppedal AL, Enakoutsab K, Cherkaoui M, Graham RH. Arockiasamy A. Acta Mater 2013;61:3923.
[4] Zhao XS, Shang SL, Liu ZK, Shen JY. J Nucl Mater 2011.
[5] Qin W, Nam C, Li H, Szpunar J. Acta Mater 2007;55:1695.
[6] Zhu WZ. Ceram Int 1996;22:389.
[7] Garvie RC, Swain MV. J Mater Sci 1985;20:1193.
[8] Garvie RC. J Mater Sci 1985;20:3479.
[9] Suresh A, Mayo MJ, Porter WD. J Mater Res 2003;18:2912.
[10] Bansal GK, Heuer AH. Acta Metall 1974;22:409.
[11] Kriven WM, Fraser WL, Kennedy SW. The martensite crystallography of tetragonal zirconia. In: Science and technology of zirconia, proc 1st int conf, Advances in ceramics. Cleveland (OH); 1980. p. 3.
[12] Kelly PM, Ball CJ. J Am Ceram Soc 1986;69:259.
[13] Muddle BC, Hannink RH. J Am Ceram Soc 1986;69:547.
[14] Navruz N. Phys Metal Metallogr 2008;105:580.
[15] Kelly PM, FrancisRose L. Prog Mater Sci 2002;47:463.
[16] Boettinger WJ, Warren JA, Beckermann C, Karma A. Annu Rev Mater Res 2002;32:163.
[17] Zaeem MA, Yin H, Felicelli SD. Appl Math Model 2012;35:3495.
[18] Wang S, Zaeem MA, Horstemeyer MF, Wang PT. Mater Technol 2012;27:355.
[19] Zaeem MA, Mesarovic SD. Comput Mater Sci 2011;50:1030.
[20] Chen LQ. Annu Rev Mater Res 2002;32:113.
[21] Asle Zaeem M, El Kadiri H, Mesarovic SD, Horstemeyer MF, Wang PT. J Phase Equilib Diffus 2011;32:302.
[22] Fan D, Chen LQ, Chen SP. J Am Ceram Soc 1998;81:526.
[23] Asle Zaeem M, El Kadiri H, Horstemeyer MF, Khafizov M, Utegulov Z. Curr Appl Phys 2011;12:570.
[24] Wang Y, Khachaturyan A. Acta Mater 1997;45:759.
[25] Chen LQ, Yang W. Phys Rev B 1994;50:15752.
[26] Asle Zaeem M, El Kadiri H, Wang PT, Horstemeyer MF. Comput Mater Sci 2011;50:2488.
[27] Cahn JW, Hilliard JE. J Chem Phys 1958;28:258.
[28] Allen SM, Cahn JW. Acta Metall 1979;27:1085.
[29] Landau LD, Collected papers of L.D. Landau. Oxford: Pergamon Press; 1965.
[30] Chen LQ, Khachaturyan A. Acta Metall Mater 1991;39:2533.
[31] Ahluwalia R, Lookman T, Saxena A, Albers RC. Acta Mater 2004;52:209.
[32] Levitas VI, Preston DL. Phys Rev B 2002;66:134206.
[33] Mamivand M, Asle Zaeem M, El Kadiri H. Comput Mater Sci 2013;77:304.
[34] Wen Y, Wang Y, Chen LQ. Acta Mater 1999;47:4375.
[35] Wen Y, Wang Y, Chen LQ. Philos Mag A 2000;80:1967.
[36] Artemev A, Wang Y, Khachaturyan A. Acta Mater 2000;48:2503.
[37] Artemev A, Jin Y, Khachaturyan A. Acta Mater 2001;49:1165.
[38] Artemev A, Jin Y, Khachaturyan A. Philos Mag A 2002;82:1249.
[39] Jin Y, Artemev A, Khachaturyan A. Acta Mater 2001;49:2309.
[40] Wang YU, Jin YM, Khachaturyan AG. Acta Mater 2004;52:1039.
[41] Koyama T, Onodera H. Mater Trans JIM 2003;44:2503.
[42] Seol DJ, Hu SY, Li YL, Chen LQ, Oh KH. Mater Sci Forum 2002;408–412:1645.
[43] Seol D, Hu S, Li Y, Chen L, Oh K. Metal Mater Int 2003;9:221.
[44] Man J, Zhang J, Rong Y, Zhou N. Metall Mater Trans A 2011;42:1154.
[45] Guo XH, Shi SQ, Ma XQ. Appl Phys Lett 2005;87:221910.
[46] Yamanaka A, Takaki T, Tomita Y. Mater Sci Eng A 2008;491:378.
[47] Wang Y, Wang HY, Chen LQ, Khachaturyan AG. J Am Ceram Soc 1995;78:657.

[48] Sakuma T. Trans Jpn Inst Metal 1988;29:879.
[49] Wolten G. J Am Ceram Soc 1963;46:418.
[50] Wang C, Zinkevich M, Aldinger F. J Am Ceram Soc 2006;89:3751.
[51] Subbarao EC, Maiti HS, Srivastava KK. Phys Status Solidi (a) 1974;21:9.
[52] Landau LD, Lifshitz EM, Statistical physics, Part 1, vol. 5, 3rd ed. London: Butterworth-Heinemann; 1980.
[53] Khachaturyan A. Theory of structural transformations in solids. New York: Wiley; 1983.
[54] Levitas VI. Int J Plast 2000;16:805.
[55] Mura T. Micromechanics of defects in solids, vol. 3. Berlin: Springer Verlag; 1987.
[56] Simha NK. J Mech Phys Solids 1997;45:261.
[57] She H, Liu Y, Wang B. Int J Solid Struct n.d.
[58] Idesman AV, Cho JY, Levitas VI. Appl Phys Lett 2008;93:043102.
[59] Cui YW, Koyama T, Ohnuma I, Oikawa K, Kainuma R, Ishida K. Acta Mater 2007;55:233.
[60] Cho JY, Idesman AV, Levitas VI, Park T. Int J Solids Struct 2012.
[61] Zaeem MA, Mesarovic SD. J Comput Phys 2010;229:9135.
[62] Asle-Zaeem M, Mesarovic SD. Solid State Phenom 2009;150:29.
[63] COMSOL Multiphysics Users' Guide. COMSOL Inc.; 2012.
[64] Bansal GK, Heuer AH. Acta Metall 1972;20:1281.
[65] Deville S, Chevalier J. J Am Ceram Soc 2003;86:2225.
[66] Deville S, Chevalier J, El Attaoui H. J Am Ceram Soc 2005;88:1261.
[67] Deville S, Guénin G, Chevalier J. Acta Mater 2004;52:5697.